INTERNATIONAL JOURNAL FOR NUMERICAL METHODS IN FLUIDS, VOL. 24, 215–232 (1997)

BOUNDARY TREATMENT AND AN EFFICIENT PRESSURE ALGORITHM FOR INTERNAL TURBULENT FLOWS USING THE PDF METHOD

SANDIP MAZUMDER AND MICHAEL F. MODEST

Department of Mechanical Engineering, The Pennsylvania State University, University Park, PA 16802, U.S.A.

SUMMARY

The generalized Langevin model, which is used to model the motion of stochastic particles in the velocity–composition joint probability density function (PDF) method for reacting turbulent flows, has been extended to incorporate solid wall effects. Anisotropy of Reynolds stresses in the near-wall region has been addressed. Numerical experiments have been performed to demonstrate that the forces in the near-wall region of a turbulent flow cause the stochastic particles approaching a solid wall to reverse their direction of motion normal to the wall and thereby, leave the near-wall layer. This new boundary treatment has subsequently been implemented in a full-scale problem to prove its validity. The test problem considered here is that of an isothermal, non-reacting turbulent flow in a two-dimensional channel with plug inflow and a fixed back-pressure. An efficient pressure correction method, developed in the spirit of the PISO algorithm, has been implemented. The pressure correction strategy is easy to implement and is completely consistent with the time-marching scheme used for the solution of the Lagrangian momentum equations. The results show remarkable agreement with both k–ϵ and algebraic Reynolds stress model calculations for the primary velocity. The secondary flow velocity and the turbulent moments are in better agreement with the algebraic Reynolds stress model predictions than the k–ϵ predictions.

KEY WORDS: PDF method; turbulent flow; wall treatment; pressure algorithm; Monte Carlo method

1. INTRODUCTION

The velocity–composition joint PDF method[1] is an important tool for the computation of reacting turbulent flows. Starting with the conservation equations for mass, momentum and compositions of various species (for a chemically reactive flow), a single transport equation can be derived for the joint probability density function of velocity and composition, $f_{u\phi}(\underline{V}, \underline{\psi}; \underline{x}, t)$, as described in Reference 1. The quantity $f_{u\phi}\mathrm{d}\underline{V}\mathrm{d}\underline{\psi}$ represents the probability that $\underline{V} \leqslant \underline{U} \leqslant \underline{V} + \mathrm{d}\underline{V}$ and $\underline{\psi} \leqslant \underline{\phi} \leqslant \underline{\psi} + \mathrm{d}\underline{\psi}$ occurs simultaneously, where $\underline{U}$ is the velocity vector, $\underline{\Phi}$ is the set of all scalars (temperature or enthalpy and concentrations) and $\underline{V}$ and $\underline{\psi}$ are independent sample space variables corresponding to $\underline{U}$ and $\underline{\phi}$ respectively. The transport equation for the joint PDF is a multidimensional partial differential equation and cannot be solved efficiently by traditional finite difference or finite volume techniques. The Monte Carlo method is used instead. In this method the fluid within the whole computational domain is discretized into representative 'particles' (or samples). These 'particles' then move with time and their motion is governed by their Lagrangian

CCC 0271–2091/97/020215–18

Received 27 November 1995
Revised 6 May 1996

momentum equations, which are recast in such a way that the forces acting on these representative 'particles' are modelled after stochastic processes. In accordance with the preceding discussion, the 'particles' are not actual fluid particles; however, using the PDF approach, their motion is modelled in such a way that their behavior, in an averaged sense, represents actual fluid behavior. The Monte Carlo algorithm is a natural way to trace the motion of these samples within the solution domain and is, therefore, adopted here.

During the last two decades the velocity–composition joint PDF method has been used effectively to predict hydrodynamic and scalar fields in free shear flow situations, namely jet flames, mixing layers and wakes.[2–5] So far, little effort appears to have been directed towards applying this method to internal flows or flows past solid surfaces. Internal flow calculations in the past, which have used the PDF method, involved a full-fledged finite volume calculation alongside the Monte Carlo calculations.[6,7] First, a fully converged steady state solution of the hydrodynamic field was obtained using a traditional turbulence model such as the k–ϵ model. This solution was used as initial condition for the Monte Carlo simulation, which was then taken to full convergence of the steady state equations. The strength of the PDF method lies in its ability to compute all moments between fluctuating quantities without any assumptions. For this reason the new mean velocity field and Reynolds stresses obtained from the Monte Carlo simulation were then fed back into the finite volume code to recalculate the pressure field. The procedure was repeated until convergence. A pressure correction based on the SIMPLE algorithm[8] was used. In the recent past, Anand *et al.*[9] have demonstrated a solution of the pressure field in conjunction with the Monte Carlo simulation using two-dimensional cross-validated splines. However, several important issues still remain unaddressed. Previous researchers have not addressed the question as to how a stochastic particle behaves as it approaches a solid wall. In this article this issue has been investigated in detail. Secondly, a pressure correction algorithm has been developed here which is completely consistent with the time-marching scheme used for tracing the stochastic particles and is more efficient than the SIMPLE-based pressure correction used by researchers in the past. The PISO algorithm, developed by Issa,[10] has been followed in the process of developing this pressure correction scheme. The advantage of the current pressure correction scheme will be discussed later in this article.

1.1. Governing equations

The governing equations presented in this subsection are the equations of motions for the stochastic particles. The formulation and modelling of the equations presented in this section are entirely due to Haworth and Pope.[5] For details the reader is referred to this reference and Reference 1.

For an isothermal, non-reacting, incompressible turbulent flow the change in velocity, ΔU_i^*, and the change in position, Δx_i^*, of a stochastic particle during a time interval Δt may be written as[5]

$$\Delta U_i^* = G_{ij}(U_j^* - \bar{U}_j)\Delta t + (C_0\epsilon)^{1/2}\Delta W_i - \frac{1}{\rho}\frac{\partial \bar{p}}{\partial x_i}\Delta t,$$

$$\Delta x_i^* = U_i^*\Delta t, \qquad (1)$$

where $\bar{p}$ is the mean pressure, ρ is the density of the medium and $\bar{U}_i$ is the mean velocity of the flow at any location x_i (or mean Eulerian velocity). Equation (1) has been structured after the generalized Langevin model.[5] The first two terms in the first equation represent the forces resulting from the fluctuating pressure gradient and viscous dissipation. The function $W_i(t)$ represents an isotropic Wiener process. It is a non-differentiable function which, when integrated over time, results in a random number drawn from a Gaussian distribution whose mean is zero and whose variance is equal to the time interval over which the function has been integrated. The first of these two terms is deterministic in nature and its effect is always to drive the particle velocity towards the mean velocity. The second term causes diffusion in velocity space and its effect is to cause the velocity fluctuations to assume a Gaussian distribution starting from an arbitrary distribution. The third term represents transport by the mean pressure gradient. The tensor G_{ij} for a general inhomogeneous turbulent flow assumes the form[5]

$$G_{ij} = \frac{\alpha_1 \delta_{ij} + \alpha_2 b_{ij}}{\tau} + H_{ijkl} \frac{\partial \bar{U}_k}{\partial x_l}, \tag{2}$$

where τ is the time scale for the dissipation of turbulent kinetic energy (often referred to as simply the 'turbulent time scale') and $\alpha_2 = 3{\cdot}78$. The quantity α_1 is given by[5]

$$\alpha_1 = -(\tfrac{1}{2} + \tfrac{3}{4} C_0) - \alpha_2 b_{ij} b_{ji} - \tau \gamma^* b_{ki} b_{il} \frac{\partial \bar{U}_k}{\partial x_l}, \tag{3}$$

where b_{ij} is the normalized anisotropy tensor and is expressed as

$$b_{ij} = \frac{1}{2} \frac{\overline{u_i' u_j'}}{k} - \tfrac{1}{3} \delta_{ij}, \tag{4}$$

where u_i' are the fluctuations in velocity. The constants in equation (3) are $C_0 = 2{\cdot}1$, $\gamma_1 = -1{\cdot}24, \gamma_2 = 1{\cdot}04, \gamma_3 = -0{\cdot}34, \gamma_4 = 0, \gamma_5 = 1{\cdot}99, \gamma_6 = -0{\cdot}76, \beta_1 = -0{\cdot}2, \beta_2 = 0{\cdot}8$, $\beta_3 = -0{\cdot}2$ and

$$\gamma^* = \gamma_2 + \gamma_3 + \gamma_5 + \gamma_6 = 1{\cdot}93. \tag{5}$$

The fourth-order tensor H_{ijkl} in equation (2) is given by

$$H_{ijkl} = \beta_1 \delta_{ij} \delta_{kl} + \beta_2 \delta_{ik} \delta_{jl} + \beta_3 \delta_{il} \delta_{jk} + \gamma_1 \delta_{ij} b_{kl} + \gamma_2 \delta_{ik} b_{jl} + \gamma_3 \delta_{il} b_{jk} + \gamma_4 b_{ij} \delta_{kl} + \gamma b_{ik} \delta_{jl} + \gamma_6 b_{il} \delta_{jk}, \tag{6}$$

where δ_{ij} is the Kronecker delta.

An important point to note here is that, since equation (1) is a Lagrangian equation, convective terms are absent in it, which implies that in the PDF approach convective transport is treated without approximation. Also, since the focus of this article is on the hydrodynamic aspects of the flow, the scalar transport equation has been omitted in the preceding discussion. The above equations will serve as the starting point for the formulation of the boundary conditions to follow.

2. BOUNDARY TREATMENT

In the past, although researchers have investigated internal flow situations, the methodology for treatment of boundary conditions has been crude and somewhat primitive in nature. In the context of the Lagrangian particle-tracing scheme discussed earlier, formulation of boundary conditions implies providing an answer to the query as to what happens to a particle as it approaches the wall. There are several possibilities. The particle could strike the wall, in which case additional questions arise as to with what angle and speed it would bounce back. In the past, two approaches have been used. In the first approach the particles were simply reflected specularly from the wall, implying a zero-shear-stress boundary condition. In the second approach, particles were made to reflect from the wall in such a way that the shear stress condition at the wall, as prescribed by standard wall functions, was satisfied. This strategy, however, violates the balance of local production, transport and dissipation of the Reynolds stresses in the vicinity of the wall. An alternative and more scientific approach would be to solve the stochastic equations all the way to the wall after appropriate modifications.

Since the velocity gradients and Reynolds stresses change rapidly near the wall, the tensor G_{ij}, which is a function of the gradient of the velocity and Reynolds stresses (equation (2)), also changes rapidly. This implies that the forces acting on a stochastic particle due to the fluctuating pressure gradient change significantly as the particle approaches the wall. The pressure fluctuations are damped out as the wall is approached and the viscous forces start to dominate. Therefore, to incorporate wall effects, attention needs to be focused on the tensor G_{ij}.

In the discussion to follow, expressions will be derived for all nine components of the tensor G_{ij} for the inertial sublayer as well as the viscous sublayer. For the purposes of the current analysis the solid wall will be assumed to lie in the x_1–x_3 plane, x_2 being the co-ordinate axis normal to the wall, as shown in Figure 1. Furthermore, it will be assumed that the predominant flow direction is along x_1 and the gradients of all hydrodynamic quantities are large in the x_2-direction. The flow domain in the x_3-direction will be considered infinite. Such a scenario is typically what would be encountered in a channel flow or tube flow or in any flow situation with a predominant flow direction and therefore encompasses the vast majority of engineering applications. In fact, the preceding criteria are identical with the validity criteria for the 'law of the wall' and therefore, the following derivation is valid for any flow situation for which the 'law of the wall' may be considered valid.

With these assumptions, after term-by-term reduction and some tedious algebraic manipulation of equations (2)–(6), the nine components of G_{ij} for the near-wall region may be expressed as

$$
\begin{aligned}
G_{11} &= \frac{\alpha_1}{\tau} + \frac{\alpha_2}{\tau} b_{11} + (\gamma_1 + \gamma_2 + \gamma_6) b_{12} \frac{\mathrm{d}\bar{U}_1}{\mathrm{d}x_2}, \\
G_{12} &= \frac{\alpha_2}{\tau} b_{12} + (\beta_2 + \gamma_2 b_{22} + \gamma_5 b_{11}) \frac{\mathrm{d}\bar{U}_1}{\mathrm{d}x_2}, \\
G_{13} &= \frac{\alpha_2}{\tau} b_{13} + \gamma_2 b_{32} \frac{\mathrm{d}\bar{U}_1}{\mathrm{d}x_2}, \\
G_{21} &= \frac{\alpha_2}{\tau} b_{21} + (\beta_3 + \gamma_3 b_{11} + \gamma_5 b_{22}) \frac{\mathrm{d}\bar{U}_1}{\mathrm{d}x_2}, \\
G_{22} &= \frac{\alpha_1}{\tau} + \frac{\alpha_2}{\tau} b_{22} + (\gamma_1 + \gamma_3 + \gamma_5) b_{12} \frac{\mathrm{d}\bar{U}_1}{\mathrm{d}x_2}, \qquad (7) \\
G_{23} &= \frac{\alpha_2}{\tau} b_{23} + \gamma_3 b_{31} \frac{\mathrm{d}\bar{U}_1}{\mathrm{d}x_2}, \\
G_{31} &= \frac{\alpha_2}{\tau} b_{31} + \gamma_6 b_{32} \frac{\mathrm{d}\bar{U}_1}{\mathrm{d}x_2}, \\
G_{32} &= \frac{\alpha_2}{\tau} b_{32} + \gamma_5 b_{31} \frac{\mathrm{d}\bar{U}_1}{\mathrm{d}x_2}, \\
G_{33} &= \frac{\alpha_1}{\tau} + \frac{\alpha_2}{\tau} b_{33} + \gamma_1 b_{12} \frac{\mathrm{d}\bar{U}_1}{\mathrm{d}x_2}.
\end{aligned}
$$

The above set of equations is valid for both the inertial sublayer and the viscous sublayer. In the following sections, equation (7) will be simplified further using the 'law of the wall' to yield simple analytical expressions for G_{ij}.

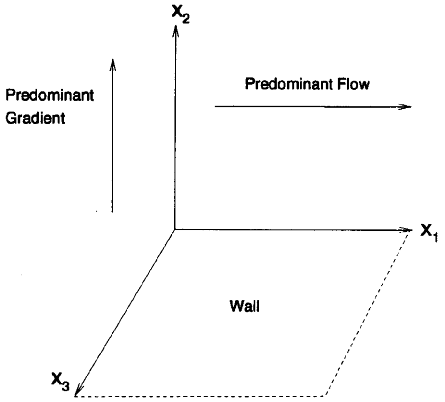

Figure 1. Co-ordinate system for near-wall analysis

2.1. *The inertial sublayer*

In terms of the notation described earlier, the log-law for the inertial sublayer may be written as[11]

$$\frac{\bar{U}_1}{U_*} = \frac{1}{\kappa} \ln\left(\frac{x_2}{\nu} U_*\right) + B, \tag{8}$$

where κ and B are constants, typically chosen to be equal to 0·4 and 5·0, respectively, and ν is the kinematic viscosity of the medium. U_* is the friction velocity and is given by the expression

$$U_* = C_\mu^{1/4} k^{1/2}, \tag{9}$$

where C_μ is a universal constant equal to 0·09 and k is the turbulent kinetic energy, typically assumed to be a constant equal to the value of the turbulent kinetic energy at the node adjacent to the wall. Upon differentiation, equation (8) yields

$$\frac{\mathrm{d}\bar{U}_1}{\mathrm{d}x_2} = \frac{U_*}{\kappa x_2}. \tag{10}$$

The time scale for the dissipation of turbulent kinetic energy, τ, is the ratio of the turbulent kinetic energy k and the rate of dissipation of the turbulent kinetic energy, ϵ. In the inertial sublayer, using Kolmogorov's equilibrium hypothesis and scaling argument, the dissipation rate may be expressed[11] as

$$\epsilon \approx \frac{U_*^3}{\kappa x_2}. \tag{11}$$

Using equations (9) and (11), the turbulent time scale may be expressed as

$$\frac{1}{\tau} = \frac{C_\mu^{3/4} k^{1/2}}{\kappa x_2}. \tag{12}$$

The task that now remains is to estimate the normalized anisotropic stress tensor b_{ij} for the inertial sublayer. Experimental data indicate that the following universal estimates[11] are valid for the inertial sublayer:

$$\overline{u_1'^2} = 4U_*^2, \qquad \overline{u_2'^2} = 0{\cdot}64U_*^2, \qquad \overline{u_3'^2} = 1{\cdot}96U_*^2, \qquad -\overline{u_1'u_2'} = U_*^2. \tag{13}$$

In addition, it will be assumed that, since the gradients in the azimuthal (x_3) direction and the mean velocity in the azimuthal direction are zero, the correlations $\overline{u'_1u'_3}$ and $\overline{u'_2u'_3}$ are small compared with the correlation $\overline{u'_2u'_2}$. This may also be justified by gradient diffusion arguments. Using equations (10) and (4), the tensor b_{ij} can be evaluated and is written in matrix form as

$$b_{ij} = \begin{bmatrix} 0{\cdot}273 & -0{\cdot}152 & 0 \\ -0{\cdot}152 & -0{\cdot}236 & 0 \\ 0 & 0 & -0{\cdot}036 \end{bmatrix}. \tag{14}$$

Substitution of equations (10), (12) and (14) into equation (7) yields the final expression for G_{ij} in the inertial sublayer:

$$G_{ij} = \begin{bmatrix} -0{\cdot}44 & 1{\cdot}27 & 0 \\ -0{\cdot}39 & -1{\cdot}67 & 0 \\ 0 & 0 & 0{\cdot}93 \end{bmatrix} \frac{k^{1/2}}{x_2}. \tag{15}$$

2.2. *The viscous sublayer*

In the viscous sublayer the primary velocity profile and its normal derivative are expressed as[11]

$$\bar{U}_1 = \frac{x_2}{v} C_\mu^{1/2} k, \tag{16}$$

$$\frac{\mathrm{d}\bar{U}_1}{\mathrm{d}x_2} = \frac{C_\mu^{1/2} k}{v}, \tag{17}$$

where v is the kinematic viscosity of the medium. In the viscous sublayer the turbulent fluctuations are damped out completely by viscosity. Hence, all Reynolds stresses are zero and the quantity $\overline{u'_iu'_j}/k$ assumes an indeterminate form. To evaluate this quantity in the viscous sublayer, one has to investigate the rate at which $\overline{u'_iu'_j}$ and k go to zero as the wall is approached. Following Hanjalic and Launder,[12] the velocity fluctuations are expanded in a series as a function of the normal distance from the wall:

$$u'_i = a_i + b_i x_2 + c_i x_2^2 + \ldots, \tag{18}$$

for $i = 1, 2, 3$, where a_i, b_i and c_i are functions of x_1, x_3 and t. Applications of 'no slip' and continuity at the wall yields

$$u'_1 = b_1 x^2 + c_1 x_2^2 + \ldots, \qquad u'_2 = c_2 x_2^2 + \ldots, \qquad u'_3 = b_3 x_2 + c_3 x_2^2 + \ldots. \tag{19}$$

Retaining terms up to leading order only, we obtain the relationships

$$\begin{aligned} &\overline{u_1'^2} = \overline{b_1^2} x_2^2 + \mathcal{O}(x_2^3), &&\overline{u_2'^2} = \overline{c_2^2} x_2^4 + \mathcal{O}(x_2^5), &&\overline{u_3'^2} = \overline{b_3^2} x_2^2 + \mathcal{O}(x_2^3), \\ &\overline{u'_1u'_2} = \overline{b_1c_2} x_2^3 + \mathcal{O}(x_2^4), &&\overline{u'_2u'_3} = \overline{c_2b_3} x_2^3 + \mathcal{O}(x_2^4), &&\overline{u'_1u'_3} = \overline{b_1b_3} x_2^2 + \mathcal{O}(x_2^3). \end{aligned} \tag{20}$$

Noting that $k = \overline{u'_iu'_i}/2$, it follows from equation (20) that $\overline{u'_iu'_j}/k$ tends to zero as x_2 tends to zero if either i or j is equal to 2.

The dominant balance of terms of the Reynolds stress transport equation in the viscous sublayer yields[13]

$$v \frac{\partial^2(\overline{u'_iu'_j})}{\partial x_k \partial x_k} = 2v \overline{\frac{\partial u'_i}{\partial x_k} \frac{\partial u'_j}{\partial x_k}} = \epsilon_{ij}. \tag{21}$$

It states that the turbulent kinetic energy, while being transported by viscous mechanisms in the viscous sublayer (the left-hand side of equation (21)), is completely dissipated (the right-hand side of equation (21)), so that at the wall the Reynolds stresses are exactly equal to zero. In equation (21) ϵ_{ij} denotes the anisotropic dissipation rate tensor. Dissipation takes place at the smallest scales of turbulence. At large Reynolds numbers the small scales of turbulence are fairly isotropic. However, near a wall the Reynolds number is small and the small scales of turbulence are anisotropic, resulting in anisotropic dissipation rates of the various components of the Reynolds stresses. Rotta[14] and later Hanjalic and Launder [12] proposed that the anisotropic dissipation tensor is equal to $\overline{u_i'u_j'}\epsilon/k$. Durbin[15] further proposed that in the extreme vicinity of the wall k tends to $\epsilon x_2^2/2\nu$. In the light of these propositions, equation (21) reduces to[15]

$$\nu\frac{\partial^2(\overline{u_i'u_j'})}{\partial x_2^2}-2\nu\frac{\overline{u_i'u_j'}}{x_2^2}=\mathcal{O}(x_2). \tag{22}$$

The solution of equation (22) yields

$$\overline{u_i'u_j'}=A_{ij}x_2^2+B_{ij}/x_2+\mathcal{O}(x_2^3), \tag{23}$$

where A_{ij} and B_{ij} are local integration constants. The Reynolds stresses are zero at the wall, which necessitates $B_{ij}=0$. Durbin[15] suggests that $A_{ij}=0$ if either i or j is equal to 2, which is consistent with the results obtained in equation (20). For the remaining components, A_{ij} may be obtained by ensuring the continuity of the Reynolds stresses at the edge of the viscous sublayer. The value of x_2 at the edge of the viscous sublayer, denoted henceforth by $x_{2\mathrm{L}}$, is a matter of choice. Typically, a value corresponding to x_{2+} of 11 is considered appropriate.[11] Using equations (4), (9), (12), (13) and (16)–(23), we obtain

$$G_{ij}=\begin{bmatrix} \dfrac{-1\cdot9\sqrt{k}}{x_2}+\dfrac{9\cdot1\nu}{x_{2\mathrm{L}}^2}-\dfrac{16\cdot4x_2\nu^2}{\sqrt{k}x_{2\mathrm{L}}^4} & \dfrac{-0\cdot6k}{\nu}+\dfrac{1\cdot7x_2\sqrt{k}}{x_{2\mathrm{L}}^2} & 0 \\ \dfrac{-0\cdot22k}{\nu}-\dfrac{0\cdot3x_2\sqrt{k}}{x_{2\mathrm{L}}^2} & \dfrac{-1\cdot9\sqrt{k}}{x_2}+\dfrac{4\cdot5\nu}{x_{2\mathrm{L}}^2}-\dfrac{16\cdot4x_2\nu^2}{\sqrt{k}x_{2\mathrm{L}}^4} & 0 \\ 0 & 0 & \dfrac{-1\cdot9\sqrt{k}}{x_2}+\dfrac{6\cdot7\nu}{x_{2\mathrm{L}}^2}-\dfrac{16\cdot4x_2\nu^2}{\sqrt{k}x_{2\mathrm{L}}^4} \end{bmatrix}. \tag{24}$$

Equation (15) or (24), along with equation (8) or (16), when substituted into equation (1), yields a set of six coupled ordinary differential equations. The solution to this set describes the path and velocity of a stochastic particle in the near-wall region. In principle, this coupled set can be solved for any given set of initial conditions. However, it appears impossible to obtain a closed-form analytical solution. In the current investigation a fourth-order Runge–Kutta solver was used to obtain a numerical solution to the set.

2.3. Behaviour of stochastic particles in the near-wall region

The first set of numerical experiments was run for a situation where the initial normal velocity $U_2^*(0)$ of the particle was varied. The streamwise initial particle velocity was set to zero, indicating that the initial motion of the particle is normal to the wall and directed towards the wall. The mean pressure gradient was set to zero. All velocities were normalized with respect to the square root of the turbulent kinetic energy. This scenario, described earlier, is one that might be encountered in flow over a flat surface or in a situation where the flow might be driven by external forces other than the mean pressure gradient. The motion of the particle was initialized at $x_{2+} = 300$, which is typically chosen as the outer edge of the inertial sublayer. The plus sign in the subscript indicates that the quantity has been normalized by ν/U_*. The mean streamwise velocity $\bar{U}_1$, as given by the log-layer at the edge of the inertial sublayer, was found to be 10·82. Under this set of conditions the worst (although rather unlikely) scenario may occur when the initial normal velocity of the particle is approximately the same as the mean streamwise velocity. Figure 2 shows the path of the particles for various initial U_2^*. As the initial U_2^* is increased, the particle penetrates deeper into the near-wall layer. For $U_2^*(0) = -12{\cdot}0$ the particle enters the viscous sublayer and reverses its path, indicating the validity of the viscous sublayer analysis. For large initial U_2^* the particle is seen to move in the direction opposite to the mean streamwise flow. In the absence of a mean pressure gradient the only force acting on the particle in the inertial sublayer is due to the fluctuating pressure gradient, which is essentially modelled as a sum of normal stresses and shear-like surface stresses. The normal stresses tend to drive the particles such that it catches up with the mean streamwise flow. However, for large U_2^* the shear-like surface stresses decelerate the particle, causing it to move in a direction opposite to the direction of the mean streamwise flow. Since the mean normal flow velocity is zero, when the particle normal velocity changes sign, the shear-like surface stresses also change sign and from that point onwards assist in the normal stresses, thereby accelerating the particle. For smaller U_2^* the shear-like stresses are not sufficiently large to decelerate the particle. For this particular case the deterministic component of the model dominates the transport of the particles and the diffusion term is small. This is indicated by the fact that the fluctuations in the path are small.

When a favourable mean pressure gradient is applied, as in the duct flows, the particles accelerate more and the negative streamwise velocities tend to become smaller in magnitude, resulting in smaller negative displacement. Furthermore, the depth to which a particle penetrates the near-wall layer is the same whether a mean streamwise pressure gradient is applied or not. In the same period of time, however, the particles move further downstream if a favourable mean pressure gradient is applied.

In a duct flow a situation that one is more likely to encounter is one where the initial streamwise particle velocity is almost the same as the streamwise mean velocity at the starting location. Furthermore, since the normal mean velocity is very small in the near-wall region, it is likely that the

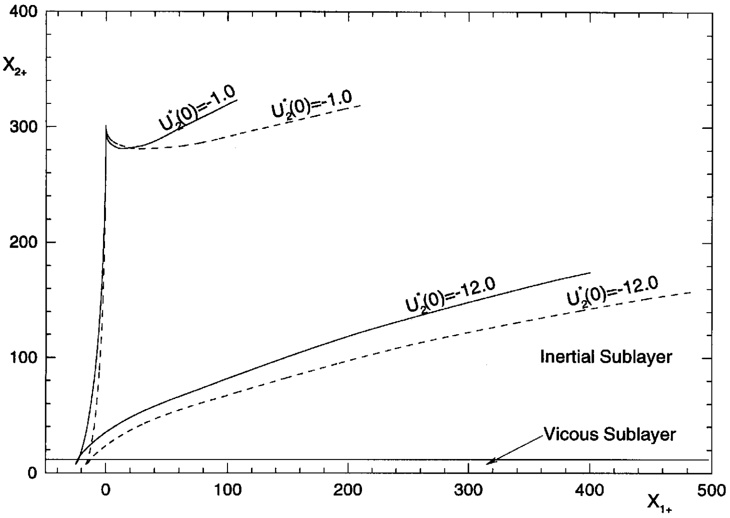

Figure 2. Particle paths in near-wall region for zero mean pressure gradient (full solid) and favourable mean pressure gradient (broken line)

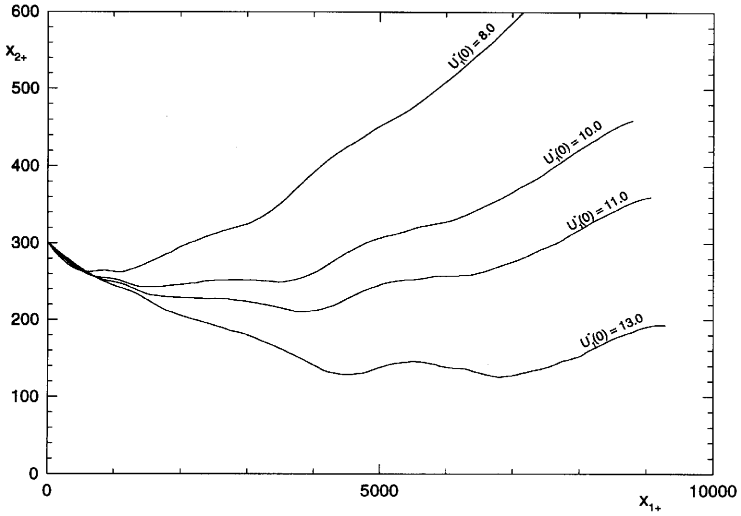

Figure 3. Particle paths in near-wall region for various initial streamwise velocities

normal particle velocity at the edge of the near-wall layer will be quite small. Figure 3 illustrates the paths of particles for various initial streamwise velocities. A normal particle velocity equal to $-1{\cdot}0$ has been used for these simulations. Once again it is observed that for each case the particle reverses its direction of motion normal to the wall. In general, if a particle of some arbitrary velocity is injected into a flow, in the absence of diffusion the particle will try to reorient itself until it has achieved the mean flow velocity. Having done so, it will simply flow along the mean flow. If the initial streamwise velocity of the particle is larger than the mean streamwise velocity, the only way that the particle can slow down to the mean flow is by moving towards the wall, whereby its streamwise velocity can decrease. This is evident in Figure 3 from the fact that, as the initial U_1^* is increased, the particle penetrates deeper into the layer. This is quite interesting, because the normal initial velocities were the same in all four cases. However, the deeper the particle penetrates, the smaller is the mean streamwise velocity, and hence it travels for larger lengths in the streamwise direction before it is able to catch up with the mean flow. This is indicated by the fact that the minima in the curves in Figure 3 shift towards the right for the cases where $U_1^*(0) > \bar{U}_1$, namely when $U_1^*(0)$ is equal to 11·0 and 13·0. In this case the paths of the particles show much more randomness, on account of the fact that the random diffusion term is comparable with the deterministic component, since the initial fluctuation is small.

Several other combinations of initial conditions are possible. For the sake of brevity, only the ones that might be commonly encountered have been discussed. The details regarding implementation of this boundary scheme in the context of a full-scale Monte Carlo simulation will be discussed later in Section 4.

3. VELOCITY–PRESSURE COUPLING

3.1. Pressure correction

In the Monte Carlo scheme the particle-tracing equations (the first equation of (1)) are in essence Lagrangian momentum equations and are marched in time. Since the velocity and pressure fields are coupled, time marching implies that the pressure changes at every time step and one should solve the momentum and continuity equations simultaneously at every time step. However, this would be an extremely time-consuming procedure. The alternative is to time march the continuity equation as well and solve for all the variables as a block. This methodology is typically adopted for transonic flows. In an incompressible flow, since the continuity equation does not have a time derivative, artificial compressibility has to be used to time march the continuity equation. This is a somewhat tricky proposition, especially in the context of Monte Carlo time stepping. An alternative way is to use a predictor–corrector scheme to correct the pressure at every time step. At a given time step $n+1$ the momentum and continuity equations will be simultaneously satisfied if and only if

$$\rho \frac{\bar{U}_i^{n+1} - \bar{U}_i^n}{\Delta t} = \mathscr{H}(\bar{U}_i^{n+1}) - \Delta_i \bar{p}^{n+1}, \tag{25}$$

$$\Delta_i \bar{U}_i^{n+1} = 0, \tag{26}$$

where the superscripts imply time indices, Δ_i is the divergence operator when acting on a vector and the gradient operator when acting on a scalar, and $\mathscr{H}$ is a function consisting of the convective, viscous and turbulent transport terms in the Reynolds-decomposed averaged Navier–Stokes equation. The exact expression for $\mathscr{H}$ is irrelevant for the purposes of this discussion. Equations (25) and (26) have to be solved implicitly and in a coupled fashion to obtain the velocity and pressure fields at the current time step $n+1$. However, in the present situation this is not feasible, because the Eulerian velocity field is not calculated directly. It is obtained instead by spatial averaging of the Monte Carlo solution. To avoid this difficulty, an approximate velocity field $\hat{U}_i$ at the current time step is first predicted by using the pressure field at the previous time step such that

$$\rho \frac{\hat{U}_i - \bar{U}_i^n}{\Delta t} = \mathscr{H}(\bar{U}_i^n) - \Delta_i \bar{p}^n. \tag{27}$$

Note that equation (27) enables us to calculate $\hat{U}_i$ explicitly. This is the first predictor step. Since $\hat{U}_i$ has been obtained by using the pressure at the previous time step, it will not in general satisfy continuity. Continuity is satisfied by seeking a new velocity field $\hat{\hat{U}}_i$ along with a new pressure field $\hat{p}$ such that

$$\rho \frac{\hat{\hat{U}}_i - \bar{U}_i^n}{\Delta t} = \mathscr{H}(\hat{U}_i) - \Delta_i \hat{p}, \tag{28}$$

$$\Delta_i \hat{\hat{U}}_i = 0. \tag{29}$$

The divergence of equation (28) yields

$$\rho \frac{\Delta_i \hat{\hat{U}}_i - \Delta_i \bar{U}_i^n}{\Delta t} = \Delta_i \mathscr{H}(\hat{U}_i) - \nabla^2 \hat{p}, \tag{30}$$

and using equation (29) and rearranging, we have

$$\nabla^2 \hat{p} = \Delta_i \mathscr{H}(\hat{U}_i) + \frac{\rho}{\Delta t} \Delta_i \bar{U}_i^n. \tag{31}$$

The corrector step consists of solving equations (31) and (28) in sequence. For an incompressible flow the quantity $\Delta_i \mathscr{H}(\bar{U}_i)$ is expressed as[1]

$$\Delta_i \mathscr{H}(\bar{U}_i) = -\rho \frac{\partial^2}{\partial x_i \partial x_j} (\bar{U}_i \bar{U}_j + \overline{u_i' u_j'}). \tag{32}$$

The second term on the right-hand side of equation (31), when integrated over a control volume, represents the mass defect of the control volume. The aforestated pressure correction strategy is very similar to the PISO algorithm,[10] except that in this case the first predictor step is explicit in time, as opposed to implicit in the original PISO algorithm. This difference places some restriction on the time step used in the time-marching scheme, especially since the function $\mathscr{H}$ is non-linear. Details regarding the choice of time step will be discussed later. Issa[10] has shown that two such predictor-corrector steps at every time step are adequate to ensure accuracy and stability of this pressure correction scheme.

To facilitate future formulations and descriptions, the following equations are written:

$$\bar{U}_i^{\mathrm{c}} = \hat{\hat{U}}_i - \bar{U}_i^n, \tag{33}$$

where $\bar{U}_i^{\mathrm{c}}$ will be referred to as the 'velocity correction' and from equation (28) is expressed as

$$\bar{U}_i^{\mathrm{c}} = \frac{\Delta t}{\rho}[\mathscr{H}(\hat{U}_i) - \Delta_i \hat{p}]. \tag{34}$$

3.2. Solution algorithm

In this subsection, a solution algorithm applicable to an elliptic flow situation will be described. In addition, important points pertaining to some of the steps in the algorithm will be highlighted to make the reader aware of the *pros* and *cons* of this solution strategy. The solution algorithm may be broadly outlined as follows.

1. The particle positions and their velocities are initialized. As opposed to what has been done by researchers in the past,[6] the mean velocity field can be set arbitrarily as long as it satisfies the global conservation laws. A good choice is to initialize the entire field with the same mean velocity everywhere. This may be achieved by setting the particle velocities as being equal to a random Gaussian deviation added to a single global mean.
2. The computational domain is broken up into cells (similar to finite volume cells). For Monte Carlo accuracy if it desirable to keep the cells as large as possible as long as the spatial truncation errors do not exceed the statistical error bounds. This is somewhat of a trial-and-error procedure.
3. The mean quantities in each cell are then computed as described by Pope.[1] For non-constant density flows, conventional means must be replaced by density-weighted (Favre) means.
4. The raw averages are then smoothed. Details on smoothing procedures can be found in De Boor's book[16] on splines and in Reference 9. This smoothing operation is an absolute necessity, as pointed out by Pope.[1]
5. All necessary gradients are computed next.
6. The particles are then marched one step in time using equation (1) and explicit time stepping. For particles close to a wall the reduced set of equations described in Section 2 is used. Details on the implementation of boundary conditions are discussed in Section 4. An arbitrary pressure gradient may be used, preferably one that is small.
7. At this stage the particles have stepped forward in time. This marks the completion of the first predictor step. Steps 4 and 5 are repeated.
8. Equation (31) is solved using any standard iterative technique and a finite volume formulation.
9. Equation (34) is solved to obtain the velocity correction and equation (33) is used to update the velocity field. This is the first corrector step.
10. Steps 4,5,8 and 9 are repeated one more time, for reasons which have been discussed in the previous section.

11. The particles are now ready to take the next step in time. However, before that, the particle velocities have to be updated as well to make them consistent with the mean updated velocity field. This is done by adding the same velocity correction as obtained in step 9 to the particle velocities at the previous time step. Since the mean and particle velocities are both corrected by the same amount, this implementation not only keeps the two velocity fields consistent but also ensures that the turbulent kinetic energy remains unchanged.
12. Steps 6–11 are repeated until a steady state solution is reached.

Since the Monte Carlo simulation is a statistical method of solution, it is difficult to detect when steady state has been reached. An effective way is to compare the pressure profiles at two successive time steps. Once steady state has been reached, the change in the pressure field will be small. The easiest way to monitor convergence is to ensure that the norm of the mass defect always stays below its value at the start of the simulation.

In the solution algorithm just described, as opposed to strategies used by researchers in the past, the necessity to run a full-fledged finite volume calculation alongside a Monte Carlo simulation is completely eliminated. The initialization of the Monte Carlo scheme is very straightforward and does not require solutions obtained from a full-scale finite volume code. The only equation that is required to be solved using a finite volume technique is the pressure Poisson equation (equation (31)). Upon finite volume discretization of equation (31) it can be seen that the coefficients for the interior nodes are functions of the cell sizes only and need to be computed only once during the entire simulation. Only the source terms and the coefficients for the cells adjacent to boundaries need to be computed at every time step. This is a distinct advantage, in addition to the fact that one does not have to take the Monte Carlo solution to full convergence for every pressure update. Furthermore, this pressure correction scheme does not require *ad hoc* specification of underrelaxation factors.

4. RESULTS OF SAMPLE CALCULATIONS

The test problem considered here is that of an isothermal, non-reacting, incompressible turbulent flow through a channel. The flow is two-dimensional in the mean, which implies that the gradients of all mean quantities in the x_3-direction are zero. The channel under consideration is 10 m long and has a height of 1 m. The inlet mean velocity is 1 m s^{-1} and has a plug profile. The density and viscosity of the fluid are then adjusted such that the Reynolds number based on the inlet velocity and channel height is 10^6. At such a high Reynolds number the channel length required to achieve fully developed flow at the exit is quite large, which would imply that the Monte Carlo simulation has to be run for a substantial length of time before steady state is reached. To avoid this problem, a moderate length of 10 m was chosen and a fixed back-pressure was specified over the entire outlet cross-section. For this particular case the back-pressure was set to zero.

For the purpose of Monte Carlo calculations the entire volume was divided into 400 spatial cells and 30,000 ‘particles’ were used. The pressure calculations were performed using the same grid. In the past,[6,9] researchers have typically used a time step equal to one-tenth of the smallest turbulent time scale for the Monte Carlo simulation. In the present case, on account of the explicit nature of the pressure correction scheme, a slightly conservative time step equal to one-thirtieth of the smallest turbulent time scale was used. To implement the boundary conditions for the Monte Carlo simulation, the following steps were adopted.

1. After every time step, all particle positions were checked to see whether any of them had crossed a solid wall.
2. If a particle had crossed the wall, then the time taken to reach the edge of the near-wall layer was calculated.

3. The position and velocities of the particle were calculated at the edge of the layer using a single explicit step in time. These served as initial conditions for calculations to be performed over the remaining part of the time step.
4. The reduced set of equations was solved using a Runge–Kutta method over the remaining part of the time step. For the sample calculations a Runge–Kutta step equal to one-hundredth of the original time step was used. However, this depends on the problem at hand and requires some degree of trial-and-error optimization. Adaptive Runge–Kutta schemes are computationally expensive, and since a Monte Carlo simulation involves several thousand particles, it is not worthwhile to use an adaptive Runge–Kutta scheme for such applications.
5. The Runge–Kutta calculations were continued until the time step was over or the particles left the near-wall layer.
6. If the particle was observed to exit the layer, the remainder of the time step was used to march the particle explicitly in time, using the exit conditions as initial conditions and the mean quantities of the local cell as the driving forces.
7. If the particle was observed to stay within the layer after a full time step, the Runge–Kutta calculations were commenced again at the beginning of the next time step.

Smoothing of the raw data obtained by averaging the Monte Carlo data was performed using two-dimensional least-squares B-splines.[16] Splines were fitted to all mean quantities that appear on the right-hand side of equation (32). Each cell was broken up into four subcells in order to provide more data points for the spline fit, and variable knots were used to fit the raw data set more accurately. In this particular case, cubic and fifth-order splines were used for the axial (x_1) and cross-stream (x_2) directions respectively. The calculation of the mass defect term in equation (31) is very critical because it ensures that continuity and momentum are satisfied simultaneously. This term can be calculated directly from Lagrangian information, as discussed by Pope.[1] However, to achieve the desired level of accuracy, it is necessary to use a very large number of particles. This issue has been addressed in detail in Reference 6. Alternatively, this term can be calculated by finite volume discretization of the mean Eulerian velocity field. This is the methodology that has been used here. However, in this study, as mentioned earlier, since a co-located grid system has been used (as opposed to a staggered grid system), simple central differencing to obtain mass fluxes at cell boundaries will result in checkerboard pressure oscillations.[17] To overcome this problem, artificial dissipation, as suggested by Rhie and Chow,[18] was added to the pressure equation. The discretized pressure equation was solved using Stone's strongly implicit method.[19] Typically it required only about 10 iterations to reduce the norm of the residuals by six orders of magnitude.

The calculation of the turbulent time scale requires the solution for ϵ at all spatial locations. This may be achieved by solution of a transport equation for ϵ. The transport equation for ϵ has to be modelled prior to its solution, and owing to the lack of adequate tools, the gradient diffusion hypothesis[11] is typically used in modelling the correlations arising from the non-linear convection transport terms. The gradient diffusion hypothesis, as pointed out by Bray and Libby,[20] is an extremely questionable hypothesis for turbulent flows with non-constant density. The solution to this problem is to include ϵ within the joint PDF itself and to solve for it as an additional scalar. Since the PDF formulation is Lagrangian, such a treatment would enable the exact treatment of convective transport terms. However, this is still a topic of current research.[21] In the current study, for the sake of simplicity, a simple algebraic model[13] has been used whereby

$$\epsilon = \frac{\mathscr{C}k^2}{\nu_{\mathrm{T}}}, \tag{35}$$

where the constant $\mathscr{C}$ is equal to 0·07 and ν_T is the kinematic eddy viscosity, which has been expressed using a modified form of the Van Driest model,

$$\nu_T = \kappa^2 x_2^2 \left[1 - \exp\left(-\frac{x^2 U_*}{\nu A^+}\right)\right]^2 \left|\frac{\partial \bar{U}_1}{\partial x_2} + \sigma\right|, \tag{36}$$

where σ was chosen to be a small number to avoid singularity in the expression for ϵ. The constant A^+ is equal to 26·0.

In the current study, results obtained from PDF calculations are compared with k–ϵ and algebraic Reynolds stress model (ARSM)[13] calculations. The ARSM calculations have also been used as a comparison for the Reynolds stress $\overline{u_1' u_2'}$. The k–ϵ and ARSM results were both obtained using the commercial code Harwell-FLOW3D with 40 × 50 finite volume cells.

Figure 4 illustrates axial mean velocity profiles at various axial locations. It is seen here that at all four axial locations the agreement of the velocity profiles obtained by the three different models is excellent. Figure 5 shows secondary velocity profiles at two different axial locations. At a distance very close to the inlet the maximum secondary velocities occur in a region very close to the wall, as shown in Figure 5(a). As the flow develops, the peak in the profile shifts towards the channel centreline. This is evident in Figure 5(b). The ARSM is observed to predict larger values for the secondary flow velocity, especially close to the inlet. It is important to note here that the PDF method

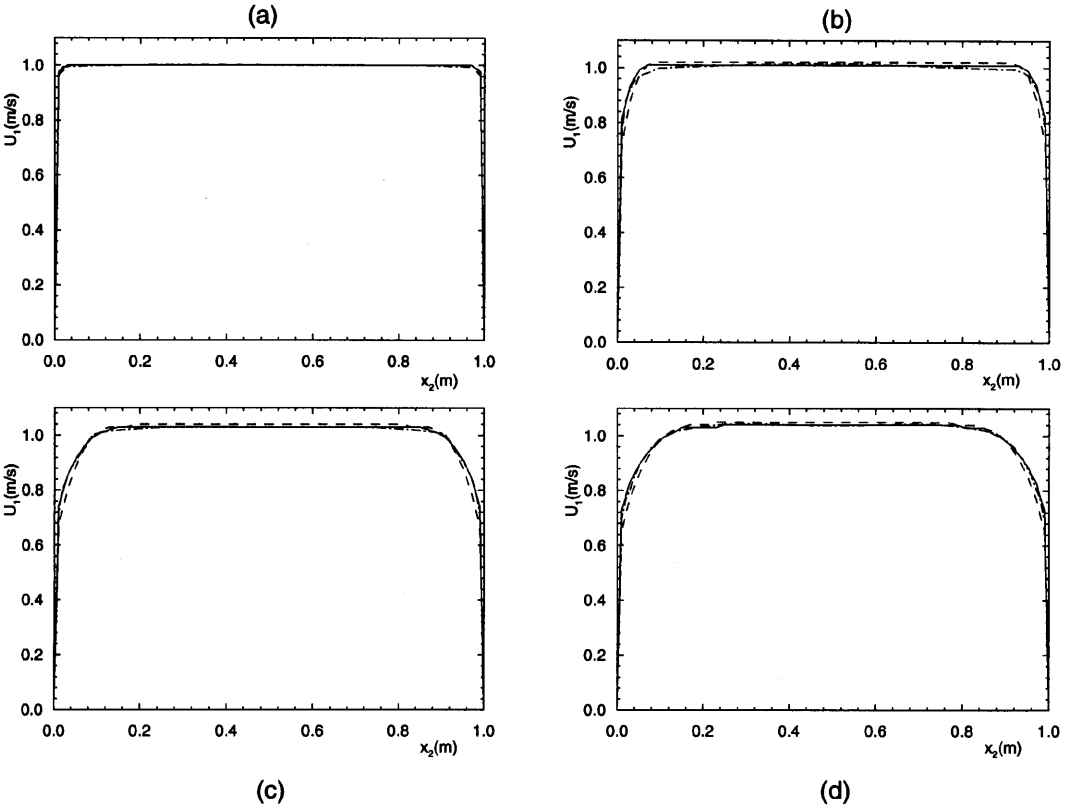

Figure 4. Mean axial velocity profiles using k–ϵ (full line), ARSM (broken line) and PDF (chain line) at (a) $x_1 = 0{\cdot}125$ m, (b) $x_1 = 2{\cdot}625$ m, (c) $x_1 = 7{\cdot}625$ m and (d) $x_1 = 9{\cdot}875$ m

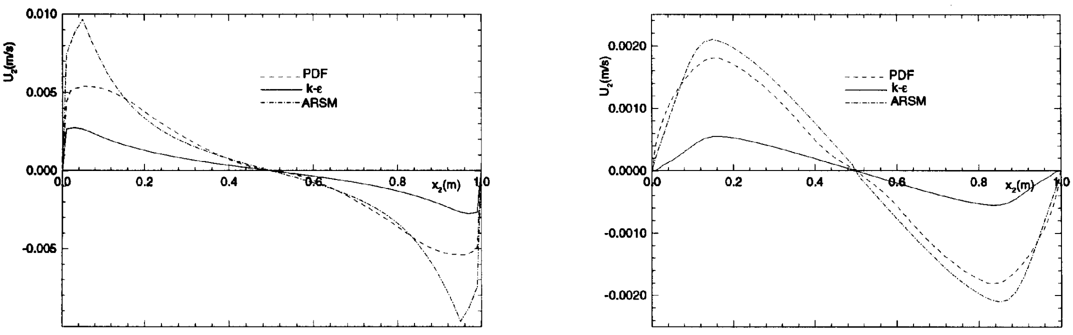

(a) (b)

Figure 5. Mean cross-stream velocity profiles at (a) $x_1 = 0{\cdot}125$ m and (b) $x_1 = 9{\cdot}875$ m

successfully predicts the shift in the peaks of the curves in going from the inlet to the exit. The profiles for the turbulent kinetic energy have been illustrated in Figure 6. The oscillations in the profiles in the region close to the channel centreline resulted from fitting splines throughout the data set. Discrepancies in the turbulent kinetic energy profiles predicted by the PDF method and the two classical methods might have also resulted from the fact that the calculation procedure for ϵ is different. It is a well-known fact that the Van Driest model is not very accurate for regions far from the walls. Figure 7 illustrates profiles for $\overline{u'_1 u'_2}$. The ARSM predicts larger Reynolds stresses than the

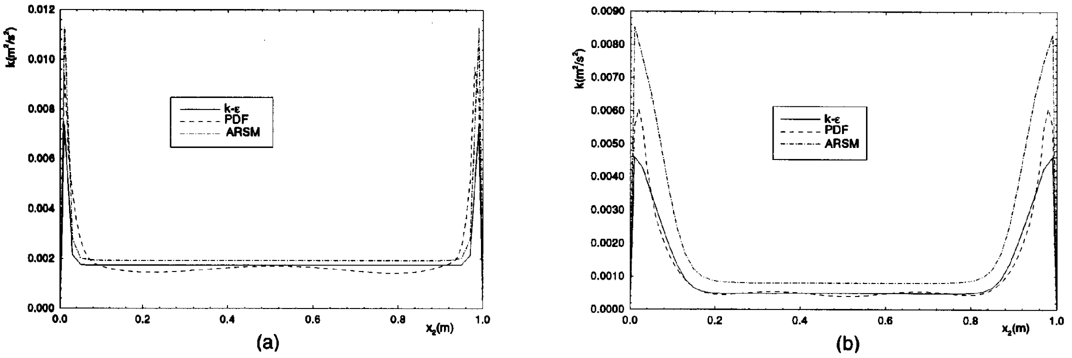

(a) (b)

Figure 6. Turbulent kinetic energy profiles at (a) $x_1 = 0{\cdot}125$ m and (b) $x_1 = 9{\cdot}875$ m

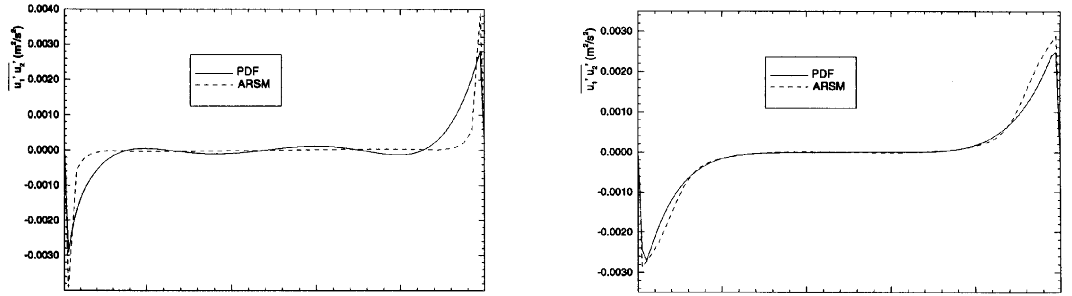

(a) (b)

Figure 7. Reynolds stress profiles at (a) $x_1 = 0{\cdot}125$ m and (b) $x_1 = 9.875$ m

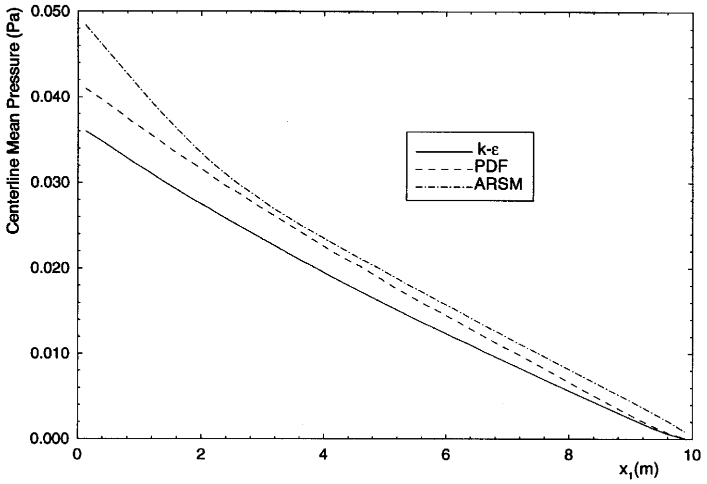

Figure 8. Centreline mean pressure

PDF method. The ARSM is formulated on the premise that the ratio $\overline{u_i'u_j'}/k$ is a constant. While more realistic than the assumptions in the k–ϵ formulation, it does not describe the redistribution of the various components of the Reynolds stresses. Figure 8 shows a comparison between centreline pressures for the different methods. The pressure drop across the whole length of the channel as predicted by the PDF and ARSM calculations is larger. One of the terms occurring in the source term of the pressure equation (32) is the cross-derivative of the Reynolds stress $\overline{u_1'u_2'}$. Thus these predictions are consistent with the Reynolds stress predictions shown in Figure 7.

5. CONCLUSIONS

The generalized Langevin model, which, to date, had only been applied to the core region of a turbulent flow, has been extended to incorporate wall effects in internal turbulent flows. It was observed that the stochastic particles never collide with the wall and retrace their paths back to the core of the flow. The methodology was applied to a full-scale two-dimensional channel flow problem and results obtained were in good agreement with k–ϵ and algebraic Reynolds stress calculations.

The PDF calculations proved more time-consuming than the k–ϵ calculations by a factor of about four. However, the motivation for using the PDF method lies in the fact that it can be applied relatively easily to problems involving a higher degree of complexity, namely turbulent reactive flows. For simple problems such as the one considered in this study, the Monte Carlo overheads (drawing random numbers, sampling the raw data set, smoothing the data set, etc.) constitute a substantial fraction of the total computational time and therefore, PDF calculations prove to be less efficient than k–ϵ calculations. With increase in complexity, these overheads increase much less in comparison with the time spent in the actual particle-tracing process and hence, the returns provided by the Monte Carlo scheme increase.

One of the fundamental problems encountered in internal flow calculations is the calculation of the pressure field. In this article a pressure algorithm based on the PISO algorithm was developed and used effectively. This pressure correction scheme derives its advantages from the fact that in the PDF method the momentum equations are marched in time, while the continuity equation cannot be marched in time for an incompressible flow. The calculation of the source terms of the pressure equation was observed to be very sensitive to the number of particles used for the simulation and the smoothing technique employed in their calculation. The smoothing procedure involves a certain degree of trial and error, and in the opinion of the present authors needs a more consistent and robust mathematical formulation than the ones currently available. This may be set as a developmental task for researchers in this area.

ACKNOWLEDGEMENT

The authors are grateful to the Applied Research Laboratory at Penn State for funding this research and for sharing their computer resources during the course of this work.

APPENDIX: NOMENCLATURE

b_{ij}	normalized anisotropy tensor
$f_{u\phi}$	velocity–composition joint PDF
G_{ij}	tensor in generalized Langevin model
H_{ijkl}	tensor appearing in expression for G_{ij}
k	turbulent kinetic energy
n	time index
$\bar{p}$	mean pressure
t	time
u_i'	velocity fluctuation
U_*	friction velocity
U_i^*	particle velocity
$\underline{U}$	instantaneous Eulerian velocity vector
$\bar{U}_i$	mean Eulerian velocity
$\bar{U}_i^{\mathrm{c}}$	velocity correction
x_i	space variable
$x_{2\mathrm{L}}$	x_2 at edge of viscous sublayer
x_i^*	position vector of particle

Greek letters

$\alpha_i, \beta_i, \gamma_i$	constants in equation for G_{ij}
ϵ	rate of dissipation of turbulent kinetic energy
ϵ_{ij}	dissipation rate tensor

REFERENCES

1. S. B. Pope, ‘PDF methods for turbulent reactive flows’, *Prog. Energy Combust. Sci.*, **11**, 119–192 (1985).
2. J. Janicka, W. Kolbe and W. Kollmann, ‘The solution of a PDF-transport equation for turbulent diffusion flames’, *Proc. Heat Transfer and Fluid Mechanics Institute, Stanford University Press, Stanford, CA, 1978.*
3. F. C. Lockwood and A. S. Naguib, ‘The prediction of the fluctuations in the properties of free, round-jet, turbulent, diffusion flame’, *Combust. Flame*, **24**, 109–124 (1975).
4. M. S. Anand and S. B. Pope, ‘Calculations of premixed turbulent flames by PDF methods’, *Combust. Flame*, **67**, 127–142 (1987).
5. D. C. Haworth and S. B. Pope, ‘A PDF modeling study of self-similar turbulent free shear flows’, *Phys. Fluids*, **30**, 1026–1044 (1987).
6. M. S. Anand, S. B. Pope and H. C. Mongia, ‘A PDF method for turbulent recirculating flows’, *Lect. Notes Eng.*, **40**, 672–693 (1989).

7. D. C. Haworth and S. H. El Tahry, ‘Application of the PDF method to in-cylinder flows in reciprocating engines’, *Proc. Seventh Symp. on Turbulent Shear Flows*, Stanford, CA, 1989.
8. S. V. Patankar and D. B. Spalding, ‘A calculation procedure for heat, mass and momentum transfer in three-dimensional parabolic flows’, *Int. J. Heat Mass Transfer,* **15**, 1787–1806 (1972).
9. M. S. Anand, S. B. Pope and H. C. Mongia, ‘Pressure algorithm for elliptic flow calculations with the PDF method’, *NASA Conf. Publ.*, **3078**, 347–362 (1991).
10. R. I. Issa, ‘Solution of the implicitly discretized fluid flow equations by operator-splitting’, *J. Comput. Phys.*, **62**, 40–65 (1985).
11. H. Tennekes and J. Lumley, *A First Course in Turbulence*, MIT Press, Cambridge, MA, 1967.
12. K. Hanjalic and B. E. Launder, ‘Contribution towards a Reynolds-stress for low-Reynolds-number turbulence’, *J. Fluid Mech.*, **74**, 593–610 (1976).
13. B. E. Launder, W. C. Reynolds and W. Rodi, *Turbulence Models and Their Applications*, Edition Eyrolles, Paris, 1984.
14. J. C. Rotta, ‘Statistiche Theorie nichthomongener Turbulenz’, *Z. Phys.*, **129**, 547 (1951).
15. P. A. Durbin, ‘A Reynolds stress model for near-wall turbulence’, *J. Fluid Mech.*, **249**, 465–498 (1993).
16. C. De Boor, *A Practical Guide to Splines,* Springer, Berlin, 1978.
17. S. V. Patankar and D. B. Spalding, *Heat and Mass Transfer in Boundary Layers*, Intertext Books, London, 1970.
18. C. M. Rhie and W. L. Chow, ‘Numerical study of the turbulent flow past an airfoil with trailing edge separation’, *AIAA J.*, **21**, 1525–1532 (1983).
19. H. Stone, ‘Iterative solution of implicit approximations of mult-dimensional partial differential equations’, *SIAM J. Numer. Anal.*, **5**, (1968).
20. K. Bray and P. Libby, ‘Counter-gradient diffusion in premixed turbulent flames’, *AIAA J.*, **19**, (1981).
21. S. B. Pope and Y. L. Chen, ‘The velocity-dissipation probability density function model for turbulent flows’, *Phys. Fluids A*, **2**, 1437–1449 (1990).